International Journal of Nanomedicine

Dovepress
Taylor & Francis Group

Open Access Full Text Article

ORIGINAL RESEARCH

Glycyrrhiza Protein-Based Nanoparticles Enhance the Oral Bioavailability and Analgesic Efficacy of Paeoniflorin

Xiaoyun Yang[1,*], Qin Guo[1,*], Yingying Dong[1,*], Huanhuan Wang[2], Mengya Dang[1], Yangyang Sun[1], Yuan Gao[1], Dong Bai[1]

[1]Institute of Basic Theory of Traditional Chinese Medicine, China Academy of Chinese Medical Sciences, Beijing, People's Republic of China; [2]School of Basic Medicine, Shaanxi University of Traditional Chinese Medicine, Xianyang, Shaanxi, People's Republic of China

*These authors contributed equally to this work

Correspondence: Yuan Gao; Dong Bai, Email gaoyuan_0714@163.com; baidong2000@126.com

Purpose: In this study, *Glycyrrhiza* protein (GP) derived from *Glycyrrhiza uralensis* Fisch was used as a carrier to prepare *Glycyrrhiza* protein Paeoniflorin nanoparticles (GP-PF NPs), and its analgesic effects, pharmacokinetic characteristics, and cellular uptake mechanisms were investigated to evaluate its potential to improve the bioavailability of PF.

Methods: We prepared GP-PF NPs through heating. A comprehensive structural characterization of the GP-PF NPs was conducted through particle size, zeta potential, electron microscopy, and spectroscopy studies, and their self-assembly mechanism was preliminarily elucidated through molecular dynamics and molecular docking. Subsequently, the analgesic effects of the GP-PF NPs and free PF were evaluated using an acetic acid writhing model, and the in vivo processes were analyzed using pharmacokinetic studies. Finally, the mechanism of transmembrane transport of GP-PF NPs was investigated in Caco-2 cells.

Results: The GP-PF NPs showed a consistent spherical shape with a 150 nm diameter and a zeta potential of −84 mV, providing excellent stability. The molecular dynamics and docking results indicated that GP-PF NPs have stable molecular dynamic characteristics. In the writhing mouse models, GP-PF NPs reduced the number of writhing events compared with the PF group, indicating stronger analgesic effect. The pharmacokinetic analysis showed that the GP-PF NPs exhibited a significant 2.60-fold increase in the maximum plasma concentration of PF and a significant 0.95-fold increase in the area under the curve of PF compared with free PF ($P<0.05$), demonstrating improved oral bioavailability. In vitro uptake and mechanistic studies showed that the GP-PF NPs were transported across membranes through caveolin-mediated endocytosis rather than passive diffusion, significantly improving the oral bioavailability of PF.

Conclusion: GP-PF NPs enhanced PF's oral bioavailability and analgesic performance by increasing intestinal absorption through caveolin-dependent endocytosis. Thus, GP may be a potential carrier for increasing the oral bioavailability of PF.

Keywords: paeoniflorin, *Glycyrrhiza* protein, nanoparticle drug delivery, oral bioavailability enhancement, caveolin-mediated endocytosis, analgesic efficacy

Introduction

Paeoniflorin (PF), a primary bioactive constituent derived from *Paeonia lactiflora*. (white peony), exhibits a broad spectrum of pharmacological activity. Accumulating evidence indicates that PF mitigates inflammation and neuropathic pain by modulating tumor necrosis factor-α (TNF-α) and interleukin-6 (IL-6) through the nuclear factor-kappa B (NF-κB) signaling pathway.[1] In addition, PF exerts neuroprotective effects by scavenging reactive oxygen species and attenuating oxidative stress.[2] Owing to its low toxicity and multitarget mechanism of action, PF is a promising candidate for integrating traditional Chinese medicine with modern therapeutic strategies.

Received: 14 May 2025
Accepted: 15 October 2025
Published: 14 November 2025

Graphical Abstract

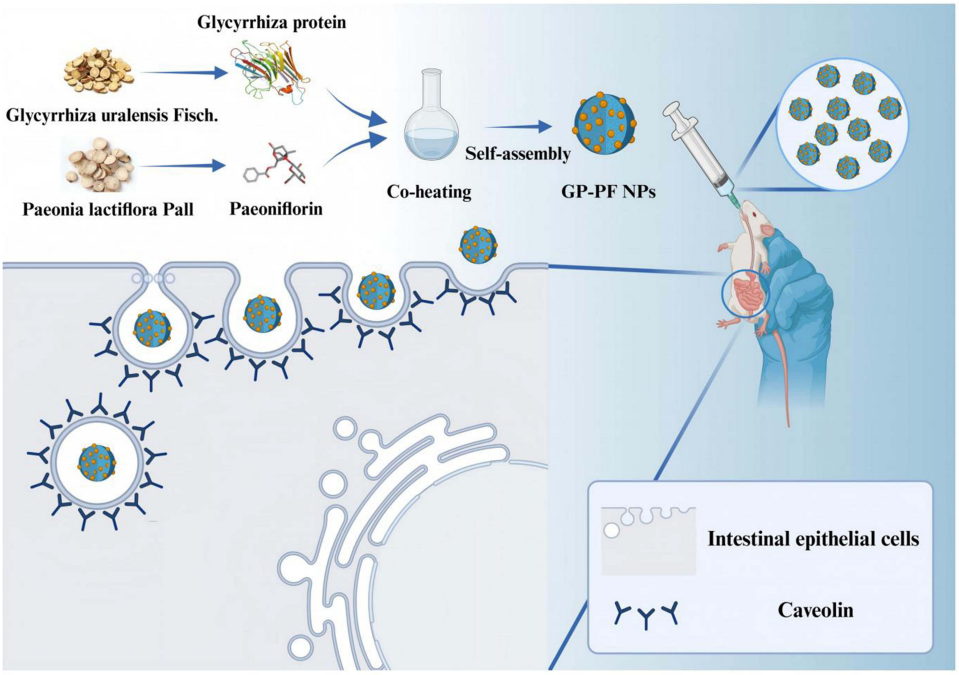

However, PF, a water-soluble monoterpene glycoside, exhibits strong hydrophilicity, poor lipophilicity, and limited transmembrane absorption, resulting in low oral bioavailability and suboptimal pharmacokinetic performance.[3] Although drug delivery systems such as liposomes[4] and polymeric nanoparticles[5] have been established to enhance its lipophilicity and increase its bioavailability,[4] conventional delivery systems face several limitations. Liposomes involve complex preparation processes[5] and are easily degraded in vivo, whereas polymer nanoparticles have poor biocompatibility and a high toxicity risk,[6] limiting their clinical application.

Recent developments have revealed that natural proteins can be effective drug delivery vehicles, owing to their abundant availability and excellent biocompatibility and safety.[7] These biomaterials possess remarkable characteristics including high biocompatibility, complete degradability, and the ability to engage in specific receptor interactions, making them particularly attractive for developing next-generation nanoparticle delivery systems.[8] For instance, plant-derived nanoparticles from soybeans, rice, and walnuts can effectively encapsulate coenzyme Q10, thereby significantly improving its stability and bioavailability.[9] Similarly, crocin-loaded protein nanoparticles derived from sorghum, foxtail millet, and pearl millet show controlled-release properties at target sites.[10]

The roots and rhizomes of *Glycyrrhiza uralensis* Fisch., a widely used medicinal herb in traditional Chinese medicine, are commonly used as decoctions for therapeutic administration. Interestingly, the decoction process facilitates the self-assembly of protein nanoparticles. Recent studies have successfully isolated and purified *Glycyrrhiza* protein (GP) from *G. uralensis*, which has a molecular weight range of 17–35 kDa.[11–13] Notably, GP has demonstrated remarkable drug delivery capabilities, effectively encapsulating various bioactive compounds including Astragaloside IV,[12] Curcumin,[14] Aconitine,[11] and dexamethasone.[13] These GP-based nanoparticles exhibit enhanced stability; significantly improved solubility, bioavailability, and therapeutic efficacy of their payloads; and reduced toxicity concerns. These findings suggest that GP is a promising natural drug delivery carrier for pharmaceutical application.

In this study, *Glycyrrhiza* protein-paeoniflorin nanoparticles (GP-PF NPs) were prepared via self-assembly and systematically characterized in terms of their physicochemical properties, including particle size, zeta potential, morphological characteristics, and intermolecular interactions. Pharmacokinetic studies in rat models combined with in vitro

absorption assays using Caco-2 cell monolayers were conducted to evaluate the enhanced absorption efficiency and improved pharmacological performance of PF delivered via GP-PF NPs. The cellular uptake mechanism was further investigated using specific endocytosis inhibitors in Caco-2 cells. This study presents a novel natural protein-based nanodelivery strategy that significantly enhances the oral bioavailability of PF.

Materials and Methods

Materials

G. uralensis Fisch. was purchased from Beijing Tongrentang Pharmacy (Beijing, China) and authenticated by Prof. Chunsheng Liu of the Beijing University of Chinese Medicine using the Pharmacopoeia of China (2025 edition). Geniposide and PF were purchased from Aladdin (Shanghai, China). Chlorpromazine (CPZ), amiloride hydrochloride, methyl-β-cyclodextrin (MβCD), and cytochalasin D were obtained from Solarbio (Beijing, China). Dulbecco's modified Eagle's medium (DMEM), phosphate-buffered saline (PBS), fetal bovine serum (FBS), and 0.25% trypsin were obtained from ProCell (Wuhan, China). The Cell Counting Kit-8 was purchased from Beyotime (Shanghai, China). Methanol and acetonitrile were obtained from Thermo Fisher (USA).

Isolation, Purification, and Identification of GP

GP (100 g) was extracted with 600 mL of phosphate buffer (0.02 M, pH 7.4) at 4°C over 12 h. The mixture was filtered using a double-layer gauze, and ethanol was added to the filtrate until the ethanol concentration reached 40% (v/v). The mixture was incubated at 4°C for 12 h and centrifuged at 3500 rpm for 20 min. Then, ethanol was added to the supernatant until the ethanol concentration was 60% (V/V). The mixture was allowed to rest at 4°C for 12 h and centrifuged at 3500 rpm for 20 min again. PBS (0.02 M, pH 7.4) was used to dissolve the precipitate, and the clear solution was the crude GP solution.

Ion-Exchange Chromatography Purification

The crude GP solution was applied to ÄKTA Purifier Protein Purifier (Cytiva, USA) equipped with a GE Healthcare XK16/20 column packed with Toyopearl SuperQ-650M resin. The column was equilibrated with 5 column volumes of PBS buffer (0.02 M, pH 7.4) at a flow rate of 1 mL/min. Subsequently, 20 mL of crude GP solution was loaded onto the column, followed by washing with two column volumes of PBS buffer (0.02 M, pH 7.4) to remove unbound proteins. Target proteins were then eluted using PBS containing 0.5 M NaCl (pH 7.4), and fractions exhibiting ultraviolet (UV) absorption at 280 nm were pooled. The combined protein fractions were dialyzed against deionized water using a dialysis membrane (MWCO 8–14 kDa) at 4°C for 12 h, during which at least five buffer changes were performed to eliminate salts. Finally, the dialyzed protein solution was lyophilized to obtain freeze-dried GP powder.

Amino Acid Composition and Protein Characterization

The GP sample was dried after hydrolysis in 6 M HCl at 110°C under a sealed nitrogen (N_2) atmosphere for 24 h and reconstituted in 0.02 M HCl and filtered using a 0.22 μm membrane. A fully automatic amino acid analyzer L-8900 (Hitachi, Japan) was used to analyze the amino acid composition of the GP by comparison of the chromatographic peaks with those of standard amino acids. *De novo* sequencing of the GP was performed using BiotechPack Scientific (Beijing, China).

Characterization of the GP

Six groups of GP solutions were prepared: native GP, heat-treated GP, GP with 0.1 M dithiothreitol (DTT), heat-treated GP with 0.1 M DDT, GP with 0.1 M Tris (2-carboxyethyl) phosphine hydrochloride (TCEP), and heat-treated GP with 0.1 M TCEP. The heat-treated groups were subjected to thermal denaturation at 100°C for 10 min. Sodium dodecyl sulfate polyacrylamide gel electrophoresis (SDS-PAGE) was performed using a 5% concentrating gel matrix and a 12% separating gel. The isoelectric point (pI) of the GP was determined by imaging capillary isoelectric focusing (iCIEF) using an ICE280 Advance full-column imaging capillary isoelectric focusing analyzer (Rongjie Biological Engineering (Suzhou) Co., Ltd., Suzhou, China). GP was mixed in a centrifuge tube with 98% methylcellulose L, an amphoteric

electrolyte, and markers 1 (pI 4.3), 2 (pI 6.8), and 3 (pI 10.0) using a wide-range pI kit (Cytiva, USA). The mixture was centrifuged at 11,000 g for 3 min and the supernatant was collected. Three pI markers served as calibration standards. The temperature of the automatic sampler was maintained at 12°C. The electrophoresis apparatus was prepared using 1.4 mL acidic electrode solution in the left chamber and 1.4 mL alkaline electrode solution in the right chamber. The focusing protocol was established as follows: Focus Period I (1 min) and Focus Period II (7 min), with a constant focusing voltage of 3,000 V. Real-time monitoring was performed using whole-column imaging detection at 280 nm, with images captured at 30-s intervals.

Preparation of the GP-PF NPs

GP and PF (mass ratio of 10:1) were dissolved in PBS (pH7.4) and stirred at 200 rpm. Then, 1% NaOH was added in the mixture until the pH reached 8.0. Subsequently, the mixture was heated at 100°C for 40 min at a speed of 300 rpm. It was then cooled to 25°C and dialyzed with 8–14 kDa MWCO for 12 h. The dialysis buffer used was distilled water, which was replaced every 3 h. The GP-PF NP powder was obtained by freezing the dialyzed solution at –80°C followed by lyophilization. The GP-PF NPs were synthesized in three separate batches to validate reproducibility.[15]

Characterization of the GP-PF NPs

The formation of the GP-PF NPs was initially verified through a qualitative assessment of the Tyndall effect. Particle size distribution together with the polydispersity index were determined by Dynamic Light Scattering (DLS) and the Zeta Potential was determined by Electrophoretic Light Scattering (ELS) using a laser particle size analyzer (Microtrac S3500, USA). The morphology of the nanoparticles was determined using transmission electron microscopy (TEM, Hitachi H-7650, Japan) and scanning electron microscopy (SEM, Zeiss Supra 55, Germany). The spectroscopic differences between the GP and GP-PF NPs were tested using UV- visible spectroscopy (vis) (Agilent, California, USA), Fourier-Transform Infrared (FT-IR) (Prestige-21, Shimadzu, Japan), proton nuclear magnetic resonance (^{1}H-NMR) (400 MHz), and ^{1}H-^{1}H- Correlation spectroscopy (COSY) (700 MHz) (Bruker, Massachusetts, USA). The experimental methods for the spectral research were as follows.

UV-vis spectra: PF solution (2 mg/mL in PBS), GP solution (2 mg/mL in PBS), and GP-PF solution were added to a colorimetric dish, and the absorbance at 200–400 nm was detected.

FT-IR spectra: Ten times the amount of KBr was added to the GP, PF, and GP-PF NPs powders (1–2 mg). After grinding and pressing, the FT-IR spectra within the range of 4000^{-1}-400 cm^{-1} were scanned.

NMR: GP, PF, and GP-PF NPs powders were dissolved in 1 mL of D_2O. The solution was then filtered and placed in a nuclear magnetic tube. The ^{1}H-NMR spectrum at 400 MHz and the ^{1}H-^{1}H-COSY spectrum at 700 MHz were recorded.

Molecular Docking

Based on the amino acid sequence of the GP, the Swiss-Model database (https://swissmodel.expasy.org/) was used for homology modeling to obtain the GP model with the highest similarity to the existing amino acid sequences in the database. The three-dimensional (3D) structures of the GP and PF were obtained from the RCSB PDB (http://www.rcsb.org/) and PubChem (https://pubchem.ncbi.nlm.nih.gov/) databases, respectively. After optimizing the 3D structure of GP using Pymol 2.3.4 software (Warren Lyford DeLano), the 3D structure of GP and PF were imported into the Auto Dock Tool software (Olson Laboratory, Scripps Research Institute, USA) to obtain the pdbqt format. Molecular docking was performed using Auto Dock Vina 1.1.2 software (Olson Laboratory, Scripps Research Institute, USA), and the results were visualized and analyzed using Pymol software (Warren Lyford DeLano).

Molecular Dynamics

AMBER 18 software was used to conduct a whole-atom molecular dynamics (MD) simulation based on the receptor-ligand structure discovered by molecular docking as the initial structure. The charge of the ligand was calculated using the antechamber module and Hartree–Fock (HF) SCF/6-31G* of the Gaussian 09 software (developed by John Pope, Carnegie Mellon University, USA). The receptor and ligand were described using the GAFF2 small-molecule force field and the ff14SB protein force field. The LEaP module was used to add hydrogen atoms to the system. A truncated

octahedral TIP3P solvent box was added at a distance of 10 Å from the system, and sodium (Na^+)/chloride (Cl^-) were added to the system to balance its charge. Finally, the topology and parameter files for the dynamic simulation were the output. A simulation of MD was performed using AMBER 18.

Biocompatibility and Safety Evaluation of the GP-PF NPs

A hemolysis assay was used to evaluate the biocompatibility of the GP-PF NPs. Briefly, 900 μL of GP-PF NP solution or GP solution at various concentrations were incubated with 100 μL of 2% (v/v) erythrocyte suspension at room temperature for 4 h. PBS and distilled water served as negative and positive controls, respectively. After incubation, the mixture was centrifuged, and the supernatant was used to measure hemoglobin release to determine the percentage of hemolysis.

A HEK-293 cell was purchased from Proell Life Science & Technology Co., Ltd (Wuhan, China) and cultured in an incubator at 37 °C and 5% CO_2. The Cell Counting Kit-8 (CCK-8) assay was used to measure the safety of the GP, PF, and GP-PF NPs in vitro. HEK-293 cells were seeded into 96-well plates at a density of 5×10^4 cells/mL. Next, various concentrations of GP, PF, and GP-PF NPs were co-cultured for 24 h. UV absorbance was measured at 450 nm using a Spark Multimode Microplate Reader (Tecen, Sweden) to calculate the survival rate of HEK-293 cells.

Acute toxicity was also evaluated in vivo. Twenty-four male Kunming (KM) mice weighing 18–20 g were randomly divided into four groups (n=6): control, PF (24 mg/kg), GP (240 mg/kg), and GP-PF NPs (24 mg/kg PF and 240 mg/kg GP). After intragastric administration, the body weight and behavior of the mice were monitored continuously. The mice were euthanized by intraperitoneal injection of 1% of pentobarbital sodium on day 14 to collect the major organs, which were preserved in 10% neutral-buffered formalin. The organs were embedded in paraffin, sectioned, and stained with hematoxylin and eosin (H&E) for histopathological examination under a light microscope. All animal procedures were approved by the Institutional Animal Care and Use Committee (IACUC) of the Institute of Basic Theory of Chinese Medicine and followed the Guidelines for the Care and Use of Laboratory Animals (ethical code number: IBTCMCACMS 21–2201-04).

Acetic Acid-Induced Writhing Test

Sixty male KM mice weighing 18–22 g were purchased from SiPeiFu Biotechnology Co. (Beijing, China) and housed in the animal experiment laboratory of the Institute of Basic Theory of Traditional Chinese Medicine, Chinese Academy of Chinese Medical Sciences, at a temperature of 23–25 °C, humidity of 55–65%, and a 12-h light/dark cycle. After 7 days of adaptive feeding with a free diet, the mice were randomly divided into six groups (n=10): control, model, APAP (150 mg/kg/day), GP (240 mg/kg/day), PF (24 mg/kg/day), and GP-PF NPs groups (240 mg/kg/day and 24 mg/kg/day PF). All groups were administered their relevant solutions intraperitoneally for 3 days with a dosage of 0.2mL/10g, and the control and model groups were given equal amounts of physiological saline. One hour after the last administration, all groups except for the control group were intraperitoneally injected with 0.1 mL/10g of 0.6% acetic acid solution, and the control group was injected with an equal amount of physiological saline. The number of twists within 15 min was recorded. All animal procedures were approved by the IACUC of the Institute of Basic Theory of Chinese Medicine and followed the Guidelines for the Care and Use of Laboratory Animals (ethical code number: IBTCMCACMS 21–2201-04).

Pharmacokinetic Study

Twelve male Sprague–Dawley (SD) rats weighing 180–200 g were purchased from SiPeiFu Biotechnology Co. (Beijing, China) and housed in the animal experiment laboratory of the Institute of Basic Theory of Traditional Chinese Medicine, Chinese Academy of Chinese Medical Sciences, at a temperature of 23–25 °C, humidity of 55–65%, and a 12-h light/dark cycle. After 7 days of adaptive feeding with a free diet, 12 SD rats were randomly divided into two groups (n=6): the PF and GP-PF NPs groups. The PF group was administered 80 mg/kg PF solution intragastrically, whereas the GP-PF NPs group was administered GP-PF NPs with an equivalent dose of PF intragastrically after 12 h of fasting. About 500 μL of blood was collected from the infraorbital plexus at 0.03, 0.25, 0.5, 0.75, 1, 2, 4, 8, 12, 24, and 48 h after administration, centrifuged at 3,500 rpm/min for 15 min to obtain plasma, and stored at −80°C. A Thermo Vanquish Flex

UHPLC system (Thermo Fisher, USA) was used to measure plasma PF (m/z=525.3) concentration, with geniposide (m/z=433.1) as the internal standard (IS). The pharmacokinetic parameters (C_max, AUC, t_1/2, MRT, etc) were calculated using Phoenix Winnonlin 8.1 software (Certara, USA). All animal procedures were approved by the IACUC of the Institute of Basic Theory of Chinese Medicine and followed the Guidelines for the Care and Use of Laboratory Animals (Ethical code number: IBTCMCACMS 21-2307-05).

Cytotoxicity Assay

The Caco-2 cell line was obtained from Proell Life Science & Technology Co., Ltd (Wuhan, China) and cultured in an incubator at 37°C and 5% CO_2. The CCK-8 assay was used to measure the cytotoxicity of PF and GP-PF NPs. The cells were detached by application of a trypsin, centrifuged at 1000 rpm for 3 min, counted by a Countstar Cell Counter (Countstar, China), resuspended at 5×10^4 cells/mL concentration in DMEM supplemented with 10% FBS, and 100 μL volumes were seeded into a 96-well flat bottom plate and incubated at 37 °C and 5% CO_2 overnight. Then, the medium was removed, and the cells were washed with PBS and replaced with 100 μL serum-free medium containing PF and GP-PF NPs at different concentrations (0.005, 0.05, 0.5, 5, 100, and 250 μg/mL). After 24 h, 10 μL of CCK-8 was added to the 96-well flat bottom plate. After incubation for 1 h, the UV absorbance at 450 nm was measured using a Spark Multimode Microplate Reader (Tecen, Sweden) to calculate the survival rate of the Caco-2 cells.

Cellular Uptake Assay

Caco-2 cells were seeded into 12-well plates at a density of 2×10^5 cells/well. To assess if the drug concentration, temperature, and incubation time play a part in cellular uptake, the cells were exposed to different concentrations (5, 25, 50, or 100 μg/mL) at different temperatures (4°C or 37°C) for different time periods (0.5, 1, 2, 4 hours), respectively. Different inhibitors including CPZ, MβCD, amiloride, and cytochalasin D were used to elucidate the uptake mode of GP-PF NPs. After treatment with different inhibitors for 2h, GP-PF NPs were added to the 12-well plates and co-cultured for 2 h.

Cell samples for PF measurement were produced through centrifugation at 12,000 rpm for 15 min at 4°C and subsequently sonicated on ice with three 15-s cycles separated by 10-s intervals.

A mixture containing 1% HCL and 100 ng/mL geniposide was added to the cell lysate and the supernatant obtained from centrifugation at 12,000 rpm for 15 min at 4°C was evaluated using QQQ (Alilent, USA).

Statistical Analysis

Statistical analyses were performed using GraphPad Prism 6.0 (GraphPad Software, USA). All data are expressed as means ± standard deviations. Comparisons among groups were performed using the one-way analysis of variance and Dunnett's post-hoc test for multiple comparisons. The significance level was set at a *P*-value of less than 0.05.

Results and Discussion

Extraction, Isolation, and Identification of the GP

The SDS-PAGE analysis showed a diffuse protein band at approximately 30 kDa in Figure 1A. The protein band of the GP exhibited reduced intensity and moved to approximately 28 kDa after heating at 100 °C for 5 min which demonstrated that heating can alter the structure of GP. Research has found that heating can alter the conformation of glycoproteins, leading to changes in SDS-PAGE bands.[16] Therefore, it is speculated that GP is a glycoprotein.

DTT and TCEP are small molecule reducing agents that can be used to reduce disulfide bonds in proteins.[17] The addition of the two reducing agents to the GP did not affect the main bands. This indicated that there are no disulfide bond in the GP (Figure 1A). The GP's pI was approximately 5.5, according to measurements from capillary isoelectric focusing, which showed observed values of 5.52, 5.57, and 5.62 (Figure 1B and Figure S1). The amino acid composition of the GP protein was quantified using an amino acid analyzer (Figure 1C). GP *de novo* sequencing proved that it was a lectin-like protein, and the amino acid sequence obtained by *de novo* sequencing was as follows:

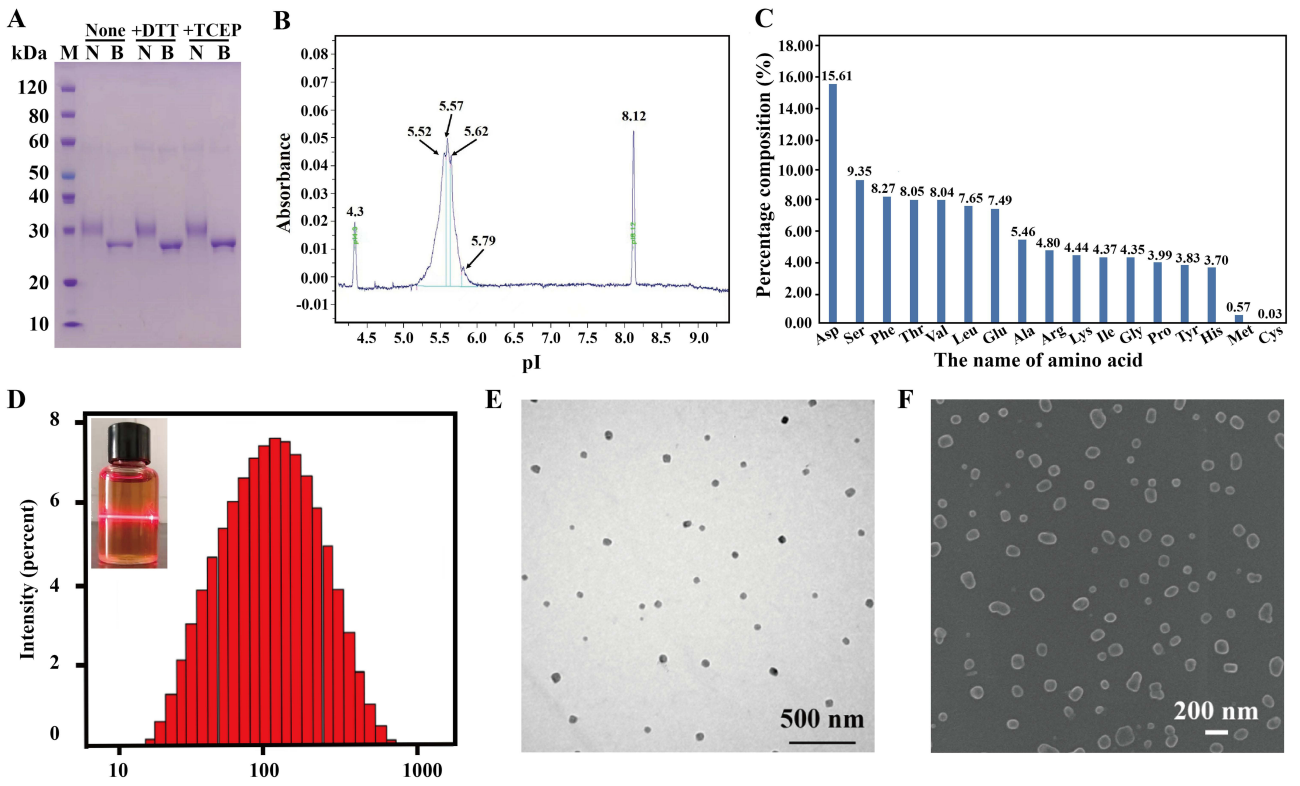

Figure 1 Characterization of GP and GP-PF NPs. (**A**) SDS-PAGE analysis of purified GP under different treatment conditions: Lane 1, native GP; Lane 2, heat-treated GP; Lane 3, GP with 0.1M DTT; Lane 4, heat-treated GP with 0.1 M DTT; Lane 5, GP treated with 0.1 M TCEP; and Lane 6, heat-treated GP with 0.1 M TCEP. (**B**) Isoelectric point diagram of GP. (**C**) Amino acid composition of GP. (**D**) Tyndall effect of GP-PF NPs in aqueous solution and particle size map of GP. (**E**) Transmission electron microscopy (TEM) images of GP-PF NPs. (**F**) Scanning electron microscopy (SEM) images of GP-PF NPs.

Abbreviations: GP, *Glycyrrhiza* protein; GP-PF NPs, *Glycyrrhiza* protein–paeoniflorin nanoparticles; SDS-PAGE, Sodium dodecyl sulfate polyacrylamide gel electrophoresis; DTT, Dithiothreitol; TCEP, Tris(2-carboxyethyl)phosphine.

ATLFNFTTFPKDHPDITLQGDASILSGGGVLALTNHAEPDSNTGRALYAEPLNIYDSDTGKIVSFQTTFTFVVD-DAGSNQYADGIAFFMAPESDAKNIPPNSGGGNLGIIDGNNAFNRLVAVEFDSYANEWDPDFTHMGIDVNSLISLK-AVRWNRESRALVHVSIVYDSASRTISVVGKSVGGVITTVSHFVDLGAVLPDKVMLGLSATTTGVRELHDIHSWS-LVSNFEDSRE

Formation and Characterization of the GP-PF NPs

As shown in Figure 1D, the Tyndall effect was observed in an aqueous solution of GP-PG NPs, which showed effective nanoparticle self-assembly. The particle size of GP-PF NPs was 148.23±0.0436 nm, which exceeds the size of the individual GP (19.96±1.7242 nm) or PF (1.02±0.0082 nm) components and their mixture (Table 1). The zeta potential of GP-PF NPs in water was −84.98±3.0795 mV, which was significantly different from that of the mixture (1.71±0.0200),

Table 1 The Particle Size and Zeta Potential of GP, PF, the Mixture of GP and PF, and GP-PF NPs

	Particle Size (nm)	PDI	Zeta Potential (mv)
PF	1.02±0.0082	0.068 ± 0.011	0.62±0.0000
GP	19.96±1.7242	0.127 ± 0.031	1.74±0.0365
Mixture	21.31±0.3001	0.421 ± 0.029	1.71±0.0200
GP-PF NPs	148.23±0.0436	0.269 ± 0.027	-(84.98±3.0795)

Notes: (n = 4, mean ± standard deviation).

Abbreviations: PF, Paeoniflorin; GP, *Glycyrrhiza* protein; GP-PF NPs, *Glycyrrhiza* protein–paeoniflorin nanoparticles; PDI, polydispersity index.

https://doi.org/10.2147/IJN.S532397

indicating that the structure changed during self-assembly. The zeta potential can be used to predict the stability of nanoparticles. When it is greater than +30 mV or less than −30 mV, it is considered a stable system. The results of SEM and TEM showed that the GP-PF NPs appeared as uniform spherical nanoparticles with a diameter of 150 nm (Figure 1E and F). Multiple parallel preparations of nanoparticles showed good uniformity in the particle size and zeta potential among batches, indicating a stable preparation method.

Spectral Analysis of the GP-PF NPs

The spectroscopic characteristics of the GP-PF NPs were studied using UV-Vis, FT-IR, and NMR spectroscopy. Compared with PF, GP-PF NPs exhibited a blue shift in the maximum absorption (from 230 nm to 220 nm) peak of the UV absorption spectrum and an increase in the maximum absorption intensity, demonstrating an interaction between GP and PF (Figure 2A). The FT-IR spectra shows (Figure 2B) that the out-of-plane bending vibration of PF's aromatic C–H shift from 711.7 cm^{-1} (PF) to 715.5 cm^{-1} (GP-PF NPs). The FT-IR spectrum of PF exhibited a characteristic wide peak at 3,200 cm^{-1}~3,600cm^{-1} for O-H stretching,[18] however, the wide peak disappeared in GP-PF NPs. Instead, an absorption bands at wave numbers of 3288 cm^{-1} appeared, which correspond to N-H stretching[18] originating from GP's secondary amide. These changes clearly demonstrated the self-assembly of GP and PF.

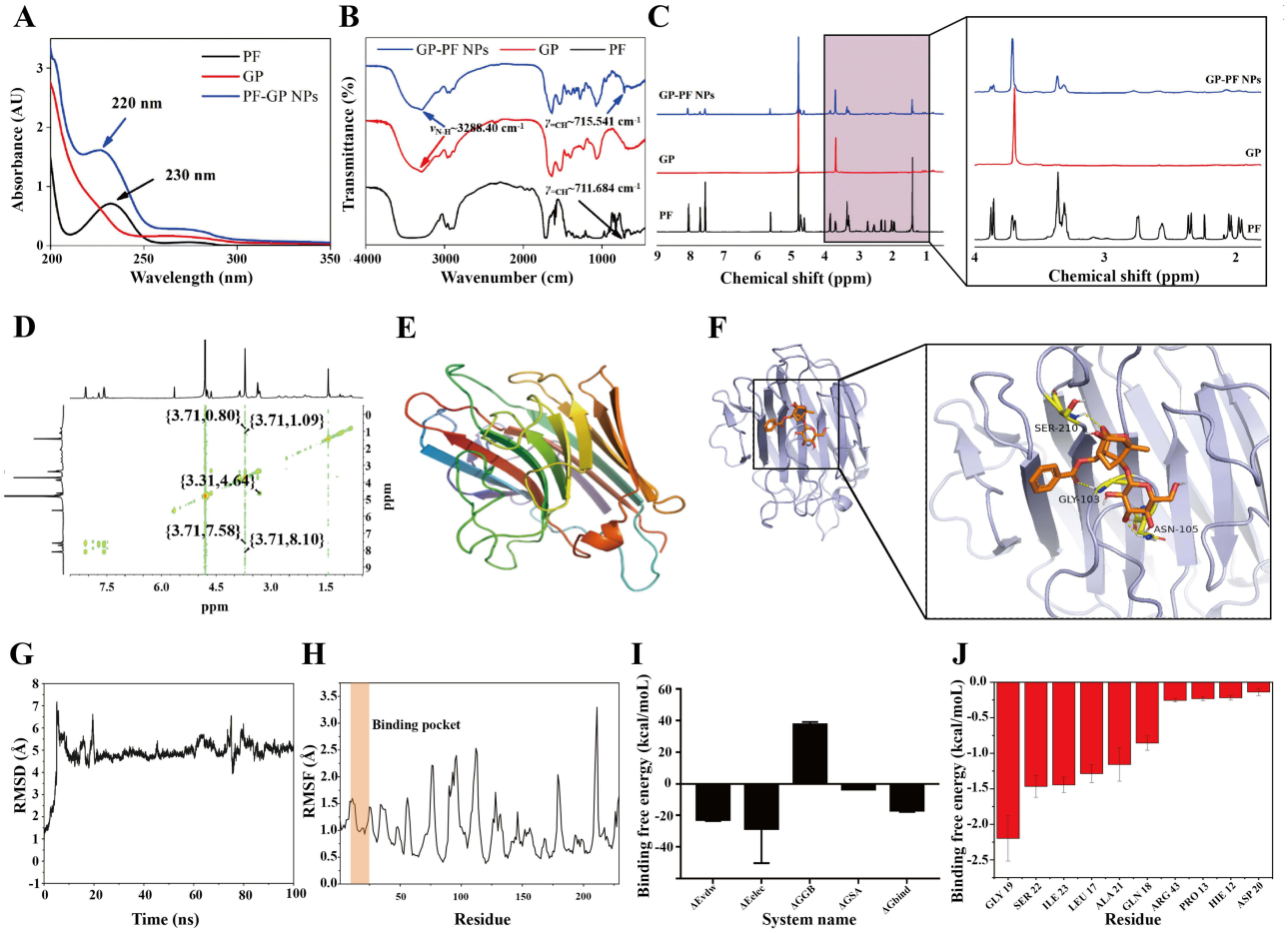

Figure 2 Self-assembly and molecular interactions of GP-PF NPs. (**A**)UV–Vis spectra of GP, PF, and GP-PF NPs. (**B**) FT-IR spectra of GP, PF, and GP-PF NPs. (**C**) ^{1}H-NMR spectra of GP, PF, and GP-PF NPs. (**D**) COSY spectra of GP-PF NPs. (**E**) Homology-modeled GP structure used for molecular docking studies. (**F**) Binding interactions of PF within GP's binding pocket, highlighting key hydrogen bonds and hydrophobic interactions. (**G**) RMSD curves of GP and PF in 100 ns molecular dynamics simulation. (**H**) RMSF analysis diagram of the GP during the 200 ns molecular dynamics simulation. (**I**) The binding free energy of the GP-PF NPs system. (**J**) Contribution of the top 10 amino acid residues to GP-PF NPs binding affinity.

Abbreviations: PF, Paeoniflorin; GP, *Glycyrrhiza* protein; GP-PF NPs, *Glycyrrhiza* protein–paeoniflorin nanoparticles; UV-Vis, Ultraviolet-visible spectroscopy; FT-IR, Fourier-transform infrared spectroscopy; NMR, nuclear magnetic resonance; COSY, Correlation spectroscopy; RMSD, root-mean-square deviation; RMSF, root-mean-square fluctuations.

The ^{1}H-NMR results for PF showed that the chemical shift between 2–4 ppm was derived from the active hydrogen of ROH in the sugar group. However, in the ^{1}H-NMR spectrum of GP-PF NPs, the chemical shift of ROH was altered, indicating that ROH in the sugar group was involved in the formation of hydrogen bonds during self-assembly (Figure 2C). The NP spectrum displayed new cross-peaks in the two-dimensional COSY NMR between the GP proton at 3.71 ppm and the PF proton at 7.55 ppm, which revealed hydrogen bonding between the GP amino groups and the PF benzoyl carbonyl group (Figure 2D). These NMR findings indicate that hydrogen bonding is essential for GP-PF NP assembly.

To further clarify the position of hydrogen bond formation between GP and PF, molecular docking and MD studies were conducted.

Molecular Docking and MD

Figure 2E shows the 3D structure of the GP obtained through homologous modeling using the Swiss Model database. Molecular docking analysis predicted that PF binds inside a pocket created by the GP residues 10–25. The primary interactions consisted of hydrogen bonds with ASP-11, ILE-23, LEU-17, and GLY-19 and hydrophobic contacts with SER-210, GLY-103, and ASN-105 (Figure 2F).

The MD simulations showed the root-mean-square deviation stabilized at approximately 5 Å after 20 ns (Figure 2G) while the root-mean-square fluctuations (RMSF) remained below 2 Å (Figure 2H) for most GP residues, indicating that the GP-PF NPs were stable The GM-PF complex revealed an estimated binding free energy of −16.9 kcal/mol (Figure 2I). GLY-19 played a major role in the binding process by forming two hydrogen bonds with PF (Figure 2J).

These results indicate that the GP-PF NPs have stable MD characteristics, among which GLY-19 mainly participates in the formation of hydrogen bonds.

Biocompatibility and Safety Evaluation of the GP-PF NPs

The hemolysis test results (Figure 3B) showed that the GP-PF nanoparticles exhibited no detectable hemolytic properties at any concentration tested; however, GP alone showed slight hemolysis at high concentrations. The conversion of GP into the nanoparticle form reduced the mild hemolytic activity observed when GP was used alone.

In vitro and in vivo experiments were performed to evaluate the safety of GP-PF NPs. The result of in vitro safety experiments (Figure 3A) showed that the GP-PF NPs were non-toxic to HEK-293 cells at concentrations ranging from 0.003–50 μg/mL. The results of the in vivo acute toxicity experiment (Figure 3C) showed that the organ and tissue structures of each group were normal and no pathological changes were observed. These findings demonstrate that GP-PF NPs exhibit excellent safety characteristics owing to their good biocompatibility and the absence of significant in vivo toxicity.

Analgesic Effects of GP-PF NPs

We established a classical writhing mouse model using 0.6% acetic acid to evaluate the analgesic effects of GP-PF NPs. GP (p=0.0081 < 0.01) or GP-PF NPs (p=0.0061 < 0.01) treatment significantly decreased writhing incidence relative to the model group, demonstrating their analgesic properties (Figure 4A). Compared with the PF group, GP-PF NPs reduced the number of writhing events in mice, indicating that GP-PF NPs have a stronger analgesic effect than PF alone. This may be because GP-PF NPs alter the pharmacokinetics and absorption process of PF in mice. Therefore, we further investigated the pharmacokinetics of PF and GP-PF NPs.

Pharmacokinetic Study

Pharmacokinetic studies evaluated the changes in blood drug concentrations over time after the administration of GP-PF and PF. Figure 4C and D showed that the quantitative detection methods for PF and the IS were specific and interference-free. Table 2 shows that the GP-PF NPs group achieved a much higher area under the concentration–time curve (AUC0–∞) of 7309.401 ± 1168.795 ng·h/L compared with 3742.341 ± 223.997 ng·h/L found in the free PF group (P < 0.05). The GP-PF NPs achieved a maximum plasma concentration of 4079.700 ± 938.679 ng/L which was 3.6 times higher than the free PF group's concentration of 1132.249 ± 226.013 ng/L (P < 0.05) (Figure 4B). The GP-PF NPs

 https://doi.org/10.2147/IJN.S532397

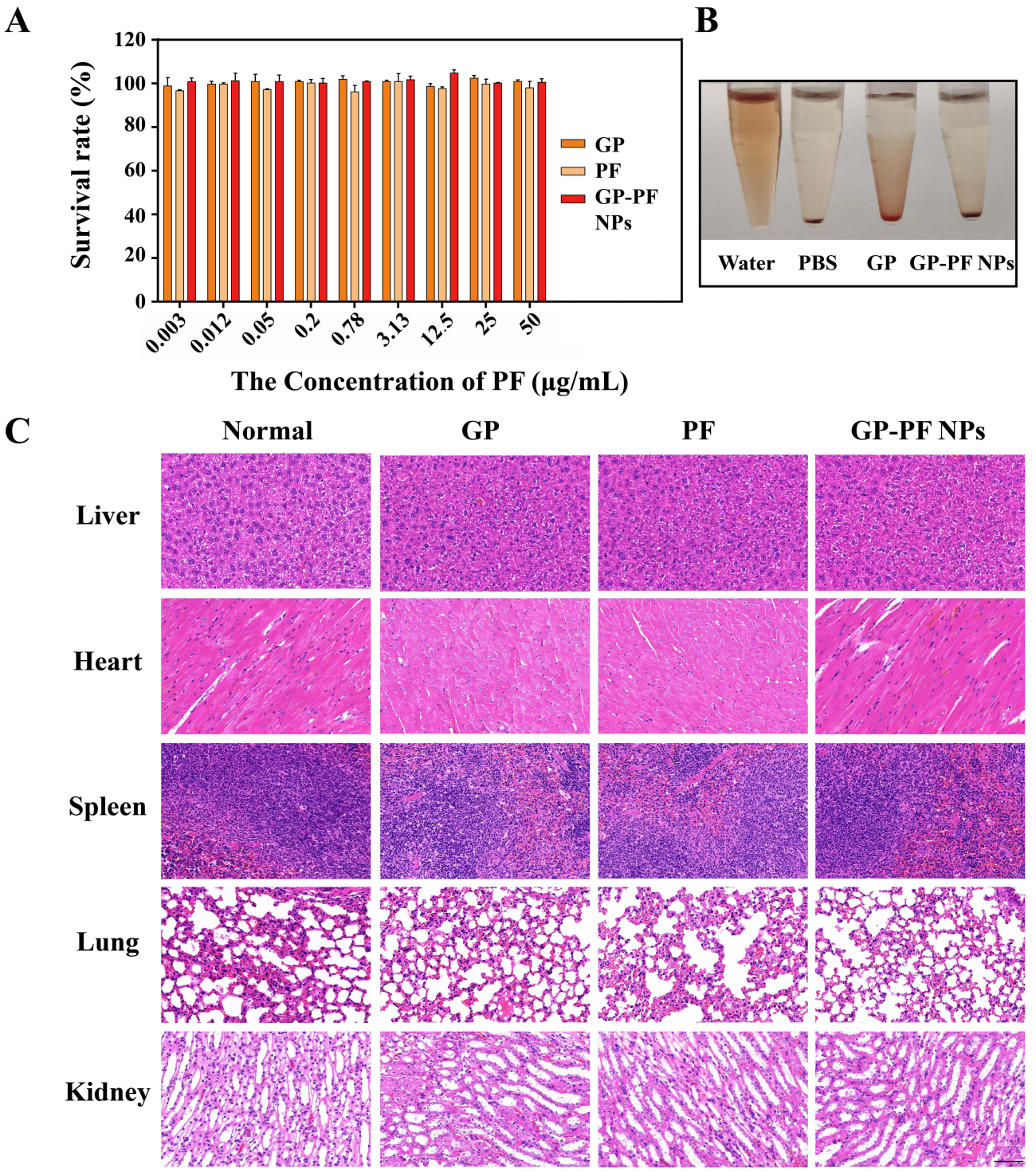

Figure 3 Biosafety evaluation of GP-PF NPs. (**A**) Cell viability of HEK-293 cells incubated with different concentrations of GP, PF, and GP-PF NPs. (**B**) Hemolysis assay of red blood cells (RBCs) treated with deionized water, PBS, and GP-PF NPs for 4 h. (**C**) Histological evaluation of tissue samples (liver, heart, spleen, lung, and kidneys) after administration of GP, PF, and GP-PF NPs, stained with H&E staining.

Abbreviations: PF, Paeoniflorin; GP, *Glycyrrhiza* protein; GP-PF NPs, *Glycyrrhiza* protein–paeoniflorin nanoparticles; PBS, phosphate buffered saline; H&E, hematoxylin and eosin.

produced no substantial changes in mean residence time (MRT) or elimination half-life (t_1/2) compared to free PF, which shows that nanoparticle formulation enhanced drug absorption instead of altering elimination kinetics. Compared with free PF, GP-PF NPs significantly increased the bioavailability and systemic exposure of oral PF, which is one of the reasons for its increased analgesic efficacy.

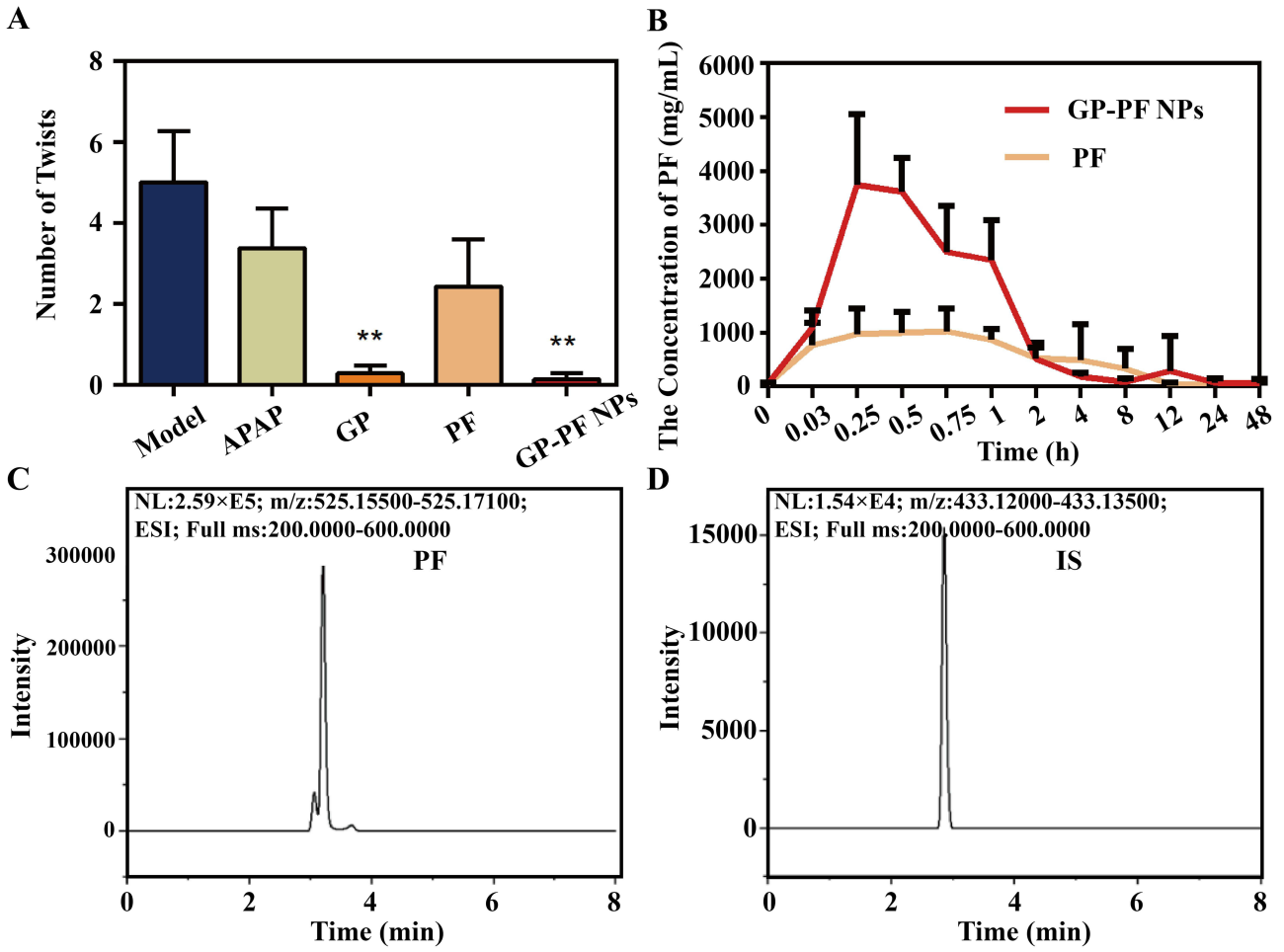

Figure 4 Pharmacological and pharmacokinetic evaluation of GP-PF NPs. (**A**) Number of writhing responses in mice over 15 min following the intraperitoneal injection of 0.6% acetic acid. Data is presented as means ± standard deviations (n=8). Compared with the model group, ** represents *P*<0.01. (**B**) Plasma concentration–time profiles of PF following oral administration of free PF solution and GP-PF NPs over 48 h in rats. Data is presented as mean ± standard deviations (n=6). (**C**)–(**D**) Representative chromatograms of PF (**C**) and the internal standard (IS) (**D**) from plasma samples.

Abbreviations: PF, Paeoniflorin; GP-PF NPs, *Glycyrrhiza* protein–paeoniflorin nanoparticles.

The absorption of small-molecule drugs in vivo primarily occurs via passive diffusion, with highly lipophilic molecules demonstrating greater permeability across cellular phospholipid bilayers.[19] However, PF exhibits strong hydrophilicity, which significantly limits passive transmembrane diffusion and contributes to poor oral bioavailability.[3]

Table 2 Pharmacokinetic Parameters of Free PF and GP-PF NPs in Sprague–Dawley Rats. (n = 6, Mean ± SD)

Parameter	Free PF	GP-PF NPs	Significance
$AUC_{(0-t)}$ (ng·h/L)	3742.341 ± 223.997	7309.401 ± 1168.795	***
$AUC_{(0-\infty)}$ (ng·h/L)	4327.503 ± 515.696	7442.593 ± 1226.926	***
$MRT_{(0-t)}$ (h)	5.130 ± 0.484	3.362 ± 3.023	ns
$MRT_{(0-\infty)}$ (h)	10.852 ± 8.312	3.924 ± 2.904	ns
$t_{1/2}$ (h)	11.422 ± 9.852	7.589 ± 2.566	ns
T_{max} (h)	0.506 ± 0.396	0.250 ± 0.006	ns
C_{max} (ng/L)	1132.249 ± 226.013	4079.700 ± 938.679	***

Note: Compared with free PF, ns represents P>0.05, *** represents P < 0.001.

Abbreviations: PF, Paeoniflorin; GP-PF NPs, *Glycyrrhiza* protein–paeoniflorin nanoparticles; AUC_{0-t}, area under the plasma concentration–time curve from 0 to the last sampling point; $AUC_{0-\infty}$, area under the curve extrapolated to infinity; MRT, mean residence time; $t_{1/2}$, elimination half-life; T_{max}, time to reach maximum plasma concentration; C_{max}, maximum plasma concentration.

https://doi.org/10.2147/IJN.S532397

Notably, nanoparticle-based drug delivery systems (100–200 nm) have been reported to facilitate intestinal epithelial transport through endocytic pathways, while evading immune surveillance.[20,21] Therefore, GP-PF NPs improved the poor lipophilicity of PF, effectively improving its oral bioavailability. To further elucidate the cellular internalization mechanism of GP-PF NPs, we employed a Caco-2 cell model to systematically investigate the endocytic pathways involved in nanoparticle uptake.

In Vitro Uptake and Mechanism Studies

The CCK-8 assay was used to determine the non-toxic dosages of GP-PF NPs and PF. The result showed that cell viability was maintained over 90% throughout 0.0005–100 μg/mL for both GP-PF NPs and PF (Figure 5A). The results (Figure 5B) show that compared with free PF, the treatment of GP-PF NPs significantly increased the cellular uptake of PF at concentrations of 50 μg/mL and 100 μg/mL (P<0.01), indicating that the GP-PF NPs can effectively enhance the uptake of PF, which is consistent with the pharmacokinetic result in vivo.

Further research was conducted to clarify the effects on PF uptake with different concentrations of GP-PF NPs on the PF uptake, temperature, and exposure time. The results (Figure 5C and D) show that the cellular uptake of GP-PF NPs increases with concentration within the range of 5–100 μg/mL, and with incubation time within 2 h. The cellular uptake of GP-PF NPs increased significantly (Figure 5E) at 37°C compared with 4°C ($P < 0.05$), which indicates that the uptake pathway of GP-PF NPs is energy dependent active transport rather than passive diffusion.[22]

A series of endocytosis inhibitors were utilized to determine the precise cellular internalization pathway of GP-PF NPs, including CPZ, a clathrin-mediated endocytosis inhibitor,[23] MβCD, a caveolin-mediated endocytosis inhibitor,[24]

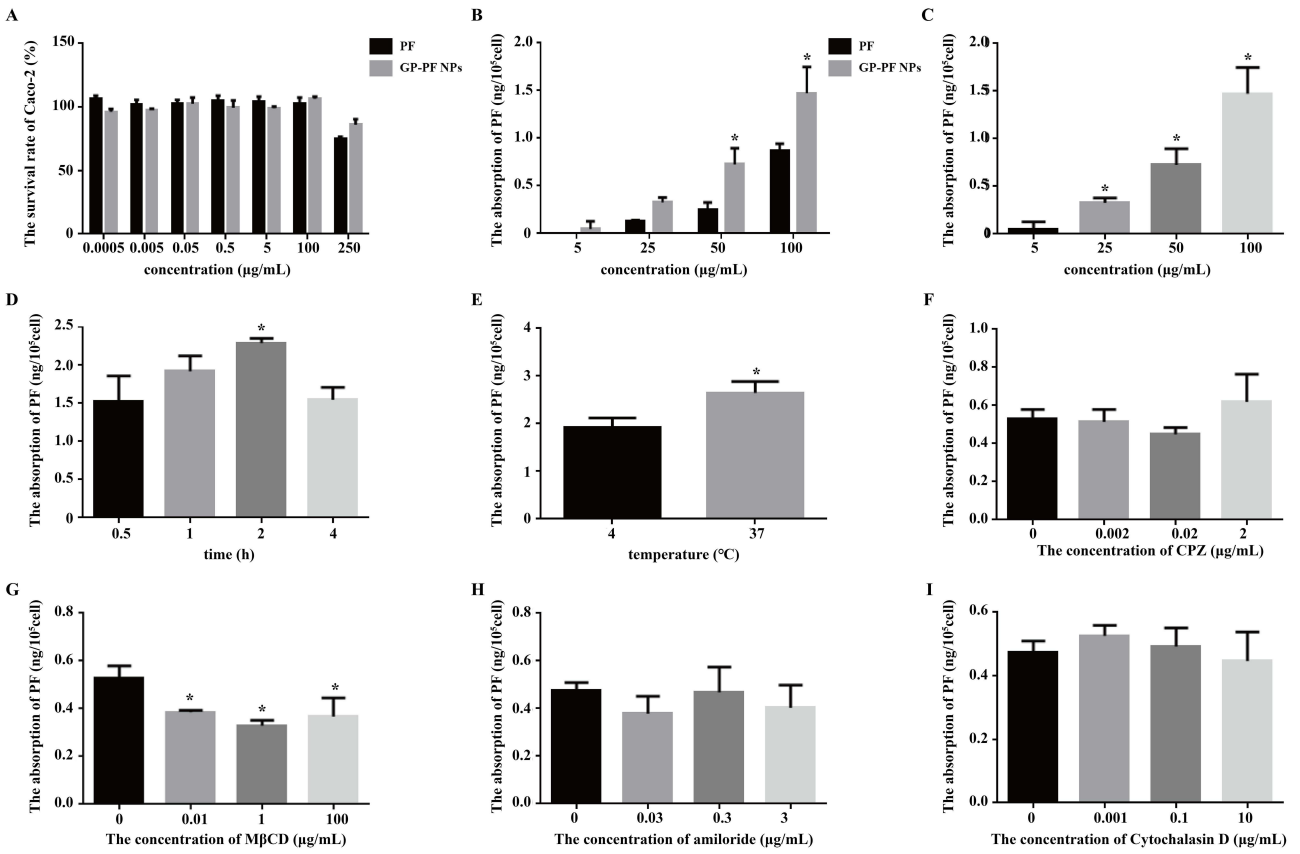

Figure 5 Cellular uptake and endocytosis mechanism of GP-PF NPs. (**A**) Survival rate of Caco-2 cells treated with different concentrations of PF and GP-PF NPs. (**B**) Cellular uptake of GP-PF NPs and PF. Compared with PF, * represents P<0.05. (**C**) Cellular uptake of GP-PF NPs at various concentrations. Compared with 5 μg/mL, * represents P<0.05. (**D**) Cellular uptake of GP-PF NPs at different time points. Compared with 0.5h, * P<0.05. (**E**) Cellular uptake of GP-PF NPs at different temperatures. Compared with 4°C, * represents P<0.05. (**F–I**) The cellular uptake of GP-PF NPs with treatment of different concentration of CPZ (**F**), MβCD (**G**), amiloride (**H**), and cytochalasin D (**I**). Compared with no inhibitors, * represents P<0.05. The concentration of GP-PF NPs was 100μg/mL.

Abbreviations: PF, Paeoniflorin; GP-PF NPs, *Glycyrrhiza* protein–paeoniflorin nanoparticles; CPZ, chlorpromazine; MβCD, Methyl-β-cyclodextrin.

amiloride, a macropinocytosis inhibitor,[25] cytochalasin D, a phagocytosis inhibitor.[26] A CCK-8 assay (Figure S2) was used to determine the non-toxic dosage of the inhibitors. The inhibitor results (Figure 5F–I) show that only MβCD treatment (Figure 5G) led to a significant reduction in GP-PF NPs uptake ($P < 0.05$).

MβCD targets membrane cholesterol, thereby removing lipid rafts, disrupting caveolae structures, and blocking caveolae-mediated endocytosis (CavME).[27] Consequently, internalization of the nanoparticles was significantly inhibited. Consistent with this mechanism, our results demonstrated that the cellular uptake of GP-PF NPs was substantially reduced upon MβCD treatment. These findings align with the established literature, which reports that the internalization of nanoparticles (100–200 nm) predominantly depends on CavME.[28,29] In contrast, other endocytic inhibitors, including CPZ, amiloride, and cytochalasin D, had minimal effects on GP-PF NPs uptake, confirming that CavME was the main pathway for GP-PF NP internalization.

These findings provide a mechanistic explanation for the enhanced bioavailability of PF delivered as GP-PF NPs. Specifically, GP-PF NPs were transported across membranes through CavME rather than passive diffusion, which effectively overcame the absorption barrier posed by PF's low lipophilicity, thereby significantly improving its oral bioavailability.

Conclusions

In this study, we successfully developed GP-PF NPs that facilitated transmembrane transport via CavME. This novel delivery system significantly enhanced the pharmacokinetic profile and oral bioavailability of PF, while concurrently improving its analgesic efficacy and demonstrating excellent safety profiles both in vitro and in vivo. This study provides new insights for improving the oral bioavailability of small-molecule drugs. Compared with liposomes and polymeric nanoparticles, natural protein-derived carriers are abundant and have good biocompatibility, making them promising drug delivery systems.

However, research on the safety of GP-PF NPs has shortcomings. It is necessary to systematically conduct research on acute and chronic toxicity to assess the safe dosage range for clinical use of GP-PF NPs. In addition, we need to be vigilant about allergic reactions associated with the in vivo application of *Glycyrrhizin*. In future studies, we will evaluate the safety of GP and nanoparticles to improve the fundamental research for their in vivo applications.

AI-Assisted Writing Disclosure Statement

This manuscript has been edited and refined with the assistance of OpenAI's ChatGPT-4o to enhance language clarity, coherence, and academic precision. The AI tool was used for grammar and style improvements, restructuring complex sentences, and refining terminology to align with scientific publishing standards. All intellectual content, data interpretation, and conclusions remain the sole responsibility of the authors. The final manuscript has been thoroughly reviewed and approved by the authors to ensure accuracy, originality, and compliance with ethical publishing standards as per Taylor & Francis AI policies (https://taylorandfrancis.com/our-policies/ai-policy/).

Abbreviations

PF, Paeoniflorin; GP, *Glycyrrhiza* protein; GP-PF NPs, *Glycyrrhiza* protein–paeoniflorin nanoparticles; CavME, Caveolin-mediated endocytosis; NF-κB, Nuclear factor-kappa B; TNF-α, Tumor necrosis factor-alpha; IL-6, Interleukin-6; KM mice, Kunming mice; SD rats, Sprague–Dawley rats; IACUC, Institutional Animal Care and Use Committee; SDS-PAGE, Sodium dodecyl sulfate polyacrylamide gel electrophoresis; DTT, Dithiothreitol; TCEP, Tris (2-carboxyethyl)phosphine; PBS, Phosphate-buffered saline; TEM, Transmission electron microscopy; SEM, Scanning electron microscopy; UV-Vis, Ultraviolet-visible spectroscopy; FT-IR, Fourier-transform infrared spectroscopy; NMR, Nuclear magnetic resonance; MD, Molecular dynamics; CPZ, Chlorpromazine (clathrin-mediated endocytosis inhibitor); MβCD, Methyl-β-cyclodextrin (caveolin-mediated endocytosis inhibitor); H&E, Hematoxylin and eosin (staining); CCK-8, Cell Counting Kit-8; AUC, Area under the plasma concentration-time curve; C_max, Maximum plasma concentration.

Ethics Approval and Informed Consent

All animal experiments were approved by the Institutional Animal Care and Use Committee of the Institute of Basic Theory of Chinese Medicine (approval numbers IBTCMCACMS 21-2201-04 and IBTCMCACMS 21-2307-05) and were performed in accordance with relevant guidelines for the care and use of laboratory animals. This article does not contain any studies with human participants. Therefore, informed consent for participation was not applicable.

Consent for Publication

Not applicable. This manuscript does not contain individual person's data in any form (including individual details, images, or videos) that would require consent for publication.

Acknowledgments

The authors thank Prof. Chunsheng Liu (Beijing University of Chinese Medicine) for his assistance in authenticating the licorice samples. Graphical abstract created in BioRender. Bai, D. (2025) https://BioRender.com/l0p0vz1.

Author Contributions

Xiaoyun Yang, Qin Guo and Yingying Dong contributed equally to this work. All authors made a significant contribution to the work reported, whether that is in the conception, study design, execution, acquisition of data, analysis and interpretation, or in all these areas; took part in drafting, revising or critically reviewing the article; gave final approval of the version to be published; have agreed on the journal to which the article has been submitted; and agree to be accountable for all aspects of the work.

Funding

This work was supported by Discipline and platform construction project of the Science and Technology Innovation project of the Chinese Academy of traditional Chinese Medicine (KYG-202409) and the The Science and Technology Innovation Project of the China Academy of Chinese Medical Sciences (CI2021A0O108).

Disclosure

Miss Yuan Gao reports a patent CN202210884691.0 licensed to Bai Dong. Professor Dong Bai reports a patent CN202210884691.0 licensed to Bai Dong. The authors declare that they have no competing interests related to this work.

References

1. Hong H, Lu X, Wu C, et al. A review for the pharmacological effects of paeoniflorin in the nervous system. *Front Pharmacol*. 2022;13:898955. doi:10.3389/fphar.2022.898955
2. Peng W, Chen Y, Tumilty S, et al. Paeoniflorin is a promising natural monomer for neurodegenerative diseases via modulation of Ca(2+) and ROS homeostasis. *Curr Opin Pharmacol*. 2022;62:97–102. doi:10.1016/j.coph.2021.11.009
3. Yang XZ, Wei W. CP-25, a compound derived from paeoniflorin: research advance on its pharmacological actions and mechanisms in the treatment of inflammation and immune diseases. *Acta Pharmacol Sin*. 2020;41(11):1387–1394. doi:10.1038/s41401-020-00510-6
4. Wang D, Yang F, Shang W, Zhao Z, Shen J, Cai H. Paeoniflorin-loaded pH-sensitive liposomes alleviate synovial inflammation by altering macrophage polarity via STAT signaling. *Int Immunopharmacol*. 2021;101(Pt A):108310. doi:10.1016/j.intimp.2021.108310
5. Naeem A, Yu C, Wang X, Peng M, Liu Y, Liu Y. Hydroxyethyl cellulose-based hydrogels as controlled release carriers for amorphous solid dispersion of bioactive components of radix paeonia alba. *Molecules*. 2023;28(21):7320. doi:10.3390/molecules28217320
6. Zielińska A, Carreiró F, Oliveira AM, et al. Polymeric nanoparticles: production, characterization, toxicology and ecotoxicology. *Molecules*. 2020;25(16):3731. doi:10.3390/molecules25163731
7. Aljabali AAA, Rezigue M, Alsharedeh RH, et al. Protein-based drug delivery nanomedicine platforms: recent developments. *Pharm Nanotechnol*. 2022;10(4):257–267. doi:10.2174/2211738510666220817120307
8. Kaltbeitzel J, Wich PR. Protein-based nanoparticles: from drug delivery to imaging, nanocatalysis and protein therapy. *Angew Chem Int Ed Engl*. 2023;62(44):e202216097. doi:10.1002/anie.202216097
9. Lin X, Chen M, Rodriguez Gonzalez P, Danino D, Corke H. Advancing coenzyme Q10 delivery with plant protein-based nanoparticle-mediated nanosuspensions. *Food Res Int*. 2024;197(Pt 1):115120. doi:10.1016/j.foodres.2024.115120
10. Jhan F, Gani A, Noor N, Ahmad Malla B, Ashwar BA. Nano reduction coupled with encapsulation as a novel technique for utilising millet proteins as future foods. *Ultrason Sonochem*. 2022;86:106006. doi:10.1016/j.ultsonch.2022.106006
11. Ke LJ, Gao GZ, Shen Y, Zhou JW, Rao PF. Encapsulation of aconitine in self-assembled licorice protein nanoparticles reduces the toxicity in vivo. *Nanoscale Res Lett*. 2015;10(1):449. doi:10.1186/s11671-015-1155-1

12. Zhou J, Zhang J, Gao G, et al. Boiling licorice produces self-assembled protein nanoparticles: a novel source of bioactive nanomaterials. *J Agric Food Chem*. 2019;67(33):9354–9361. doi:10.1021/acs.jafc.9b03208
13. Liu X, Ou X, Zhang T, et al. In situ neutrophil apoptosis and macrophage efferocytosis mediated by Glycyrrhiza protein nanoparticles for acute inflammation therapy. *J Control Release*. 2024;369:215–230. doi:10.1016/j.jconrel.2024.03.029
14. Wang H, Song B, Zhou J, et al. Fabrication and characterization of curcumin-loaded nanoparticles using licorice protein isolate from radix glycyrrhizae. *Int J Biol Macromol*. 2024;255:128235. doi:10.1016/j.ijbiomac.2023.128235
15. Guo Q. Exploring the material basis of compatibility between peony and licorice based on protein self-assembly. *Master*. 2022. https://link.cnki.net/doi/10.27658/d.cnki.gzzyy.2022.000304.
16. Chai J, Zhao X, Xu Y, Xu X. An unfolding/aggregation kinetic instructed rational design towards improving graft degree of glycation for myofibrillar protein. *Food Chem*. 2024;446:138876. doi:10.1016/j.foodchem.2024.138876
17. Li R, Xiong YL. Disulfide cleavage to improve interfacial behavior and emulsification properties of oat protein. *Food Chem*. 2023;404(Pt A):134511. doi:10.1016/j.foodchem.2022.134511
18. Aldawsari MF, Alhowail AH, Anwer MK, Ahmed MM. Development of diphenyl carbonate-crosslinked cyclodextrin based nanosponges for oral delivery of baricitinib: formulation, characterization and pharmacokinetic studies. *Int J Nanomed*. 2023;18:2239–2251. doi:10.2147/ijn.S405534
19. Schwarzinger J, Adelsberger S, Ortmayr K, et al. Biopharmaceutical profiling of anti-infective sanggenons from Morus alba root bark for inhalation administration. *Int J Pharm X*. 2024;8:100272. doi:10.1016/j.ijpx.2024.100272
20. Behzadi S, Serpooshan V, Tao W, et al. Cellular uptake of nanoparticles: journey inside the cell. *Chem Soc Rev*. 2017;46(14):4218–4244. doi:10.1039/c6cs00636a
21. Zhu Y, Fu Y, Zhang A, et al. Rod-shaped nintedanib nanocrystals improved oral bioavailability through multiple intestinal absorption pathways. *Eur J Pharm Sci*. 2022;168:106047. doi:10.1016/j.ejps.2021.106047
22. Wang F, Hang L, Dai B, et al. Characterization of herpetrione amorphous nanoparticles stabilized by hydroxypropylmethyl cellulose and its absorption mechanism in vitro. *Int J Biol Macromol*. 2024;268(Pt 1):131744. doi:10.1016/j.ijbiomac.2024.131744
23. Song S, Wang Y, Wang H, et al. Fucoidan-induced reduction of lipid accumulation in foam cells through overexpression of lysosome genes. *Int J Biol Macromol*. 2024;263(Pt 2):130451. doi:10.1016/j.ijbiomac.2024.130451
24. Zhou Y, Chen W, Zhang Y, et al. Caveolin-1 negatively regulates the calcitonin receptor-like receptor and neuroinflammation in a female mouse model of migraine. *J Neuroinflammation*. 2025;22(1):134. doi:10.1186/s12974-025-03466-8
25. Malka M, Czaczkes I, Kashkash S, Shachar S, Bacharach E, Ehrlich M. Inhibition of early EHDV2-Ibaraki infection steps in bovine cells by endosome alkalinization or ikarugamycin, but not by blockage of individual endocytic pathways. *Front Cell Infect Microbiol*. 2025;15:1494200. doi:10.3389/fcimb.2025.1494200
26. He X, Li Z, Li S, et al. Huoxue Tongluo tablet enhances atherosclerosis efferocytosis by promoting the differentiation of Trem2(+) macrophages via PPARγ signaling pathway. *Phytomedicine*. 2025;140:156579. doi:10.1016/j.phymed.2025.156579
27. Biswas A, Kashyap P, Datta S, Sengupta T, Sinha B. Cholesterol depletion by MβCD enhances cell membrane tension and its variations-reducing integrity. *Biophys J*. 2019;116(8):1456–1468. doi:10.1016/j.bpj.2019.03.016
28. He Y, Cheng M, Yang R, et al. Research progress on the mechanism of nanoparticles crossing the intestinal epithelial cell membrane. *Pharmaceutics*. 2023;15(7):1816. doi:10.3390/pharmaceutics15071816
29. Baranov MV, Kumar M, Sacanna S, Thutupalli S, van den Bogaart G. Modulation of immune responses by particle size and shape. *Front Immunol*. 2020;11:607945. doi:10.3389/fimmu.2020.607945